Developing a new permeability model of the compressible tailings thickening bed based on the pore network structure parameter

Gezhong Chen [a,d], Cuiping Li [a*], Zhuen Ruan [a,b,d*], Raimund Bürger [c], Hezi Hou [a,d]

a. *Key Laboratory of the Ministry of Education of China for High-efficient Mining and Safety of Metal Mines, University of Science and Technology Beijing, Beijing 100083, PR China*

b. *Shunde Innovation School, University of Science and Technology Beijing, Foshan 528399, PR China*

c. *CI²MA and Departamento de Ingeniería Matemática, Facultad de Ciencias Físicas y Matemáticas, Universidad de Concepción, Casilla 160-C, Concepción, Chile*

d. *School of Civil and Resource Engineering, University of Science and Technology Beijing, Beijing 100083, PR China*

*Corresponding authors: E-mail: cpli@ustb.edu.cn (C Li), E-mail: ustb_ruanzhuen@hotmail.com (Z Ruan).

Abstract

In the tailings thickening process, the low-concentration tailings slurry is separated by solid-liquid separation, forming a compressible tailing thickening bed structure at the bottom of the thickener. This structure provides a high-concentration filling slurry for mine paste backfilling production. Microstructure study of the compressible tailings thickening bed and analysis of its permeability is essential for preparing high-concentration filling slurry and ensuring stable equipment operation. In this study, we employed computer tomography to obtain the pore structure of the compressible tailings thickening bed at different pressures with and without shear. We analyzed the evolution of the compressible tailings thickening bed pore structure under mechanical action based on the pore network model (PNM). Permeability simulation experiments of the compressible tailings thickening bed structure were conducted to obtain the permeability evolution trend. Based on the PNM model of the compressible tailings thickening bed pore structure and the research on the thickening bed permeability, a new quantitative index T_w was proposed, and a new permeability model was constructed, considering the throat structure parameters. Three empirical models were used to predict the compressible tailings thickening bed permeability and were compared with the simulation results and the new model. The results indicate that the compressible tailings thickening bed porosity decrease with increasing thickening

bed pressure, which reduces the permeability of the compressible tailings thickening bed structure while increasing the concentration of the thickening bed slurry. In comparison to without shear, rake shear action caused forced damage to the compressible tailings thickening bed pore structure, forcing further discharge of fluid in the tailings thickening bed structure, resulting in an additional increase in tailings thickening bed slurry concentration and a further decrease in permeability. The diameter of the spherical pores and the diameter and length of the stick throat in the compressible tailings thickening bed structure all decrease with the increase in the thickening bed pressure. Fluid in the compressible tailings thickening bed structure primarily discharged to the top of the thickening bed through the throat structure in the PNM model, and the compressible tailings thickening bed structure permeability decreases with increasing T_w value of the throat. The new model proposed in this study, considering the throat structure parameter T_w, is more accurate in predicting the compressible tailings thickening bed permeability compared to the empirical model.

Keywords: tailings thickening; thickening bed; pore network model; permeability

Nomenclature		A_{pc}	Area of the connected throat on the cross-section (μm^2)
T_w	Structural parameters of the throat	A_{pi}	Area of the isolated throat on the cross-section (μm^2)
T_{wave}	Average structural parameters of the throat	φ_c	Pore connectivity (%)
L_c	Throat channel length (μm)	$\lambda_{\max}$	Maximum pore diameter (μm)
L_{ave}	The average throat channel length (μm)	D_T	The fractal dimension for tortuosity
D_c	Throat equivalent diameter (μm)	h_i	Height of the thickening bed in section *i* (cm)
D_{ave}	The average throat equivalent diameter (μm)	ω_i	Concentration of thickening bed in section *i* (%)
D_p	Diameter of spherical pore (μm)	α	Coefficient (4.1)
Q	The flow through the thickening bed (μm^3·s^{-1})	β	Coefficient (2.96)
K	Permeability of the compressible tailings thickening bed (d)	k	KC Constant (5、3.5)
A_t	Cross-sectional area of the thickening bed (μm^2)	d_p	Particle diameter (μm)
△P	Pressure difference of the thickening bed (Pa)	τ	Tortuosity of pores
μ	Viscosity of the fluid (Pa·s)	D	The diameter of sample (μm)
L_s	Height of the compressible tailings thickening bed (μm)	γ	The skewness of PSD
q_i	Fluid flow in a single throat (μm^3·s^{-1})	C_d	The coefficient of variation of PSD
V_t	Total volume of compressible tailings thickening bed (μm^3)	C_k	The microstructure coefficient
Φ	Porosity of the compressible tailings thickening bed (%)	S_m	The movable fluid saturation
V_{pc}	The volume of the connected pores (μm^3)	D_{Tm}	The tortuosity fractal dimension of movable fluid space
n	Number of throats in the thickening bed interface	D_{Tt}	The tortuosity fractal dimension of total pore space
A_s	Area of solid particles in the thickening bed interface (μm^2)	a_1	Coefficient
D_f	Fractal dimension of the pore structure	b_1	Coefficient
Φ_i	Porosity of thickening bed in section *i* (%)	c_1	Coefficient

1. Introduction

Separation and purification technology, as a standard means of solid and liquid separation in mixture materials, has been successfully applied in mining engineering [1], pharmaceutical engineering [2], the papermaking industry [3], chemical engineering [4], biological engineering [5], and other fields. It provides an effective means for underground oil extraction [6], rare metal extraction [7], wastewater treatment [8], and product concentration [9], among others, and has yielded significant economic benefits.

As one of the important ways of solid-liquid separation, seepage has attracted the research interest of many scholars, and various permeability models have been developed for porous media materials with varying properties. The Kozeny-Carman (KC) model, based on the Hagen-Poiseuille equation and Darcy's law, is the most classical, but the KC model has limitations [10]. Researchers such as Bourbie [11] and Civan [12] modified the parameters of KC model according to different research targets, which improved the prediction of permeability in porous media. Xu and Yu [13] modified the KC model based on the fractal dimension theory and derived a permeability model without empirical parameters. However, there have been relatively few studies in previous research on the compressible, non-homogeneous tailings thickening bed structure and the compressible tailings thickening bed permeability based on multi-scale tailings particle size. Therefore, it is necessary to conduct micro-structure studies of compressible, non-homogeneous tailings thickening beds to fill this gap. Additionally, the flow state of the fluid in the compressible, non-homogeneous tailings thickening bed structure should be quantitatively analyzed to guide industrial production.

Permeability k is considered an important parameter for evaluating the flow state of fluid in porous media and the ability of the fluid to pass through the porous medium [14]. To make a more reasonable comparison with the permeability model proposed in this study, we summarize the permeability model of porous media formed by particles, as shown in Table 1. The parameters of the theoretical model show that the flow state of the fluid in the porous medium is not only related to the porosity of the solid material but also to the pore diameter, tortuosity, connectivity, and pore fractal dimension [14–20]. However, the particle size of the porous media studied by the previous permeability model was single, and the particle size distribution in industrial production is wide. Porous media formed by a single particle size does not match the actual situation in industrial

production. In addition, the current permeability model is not suitable for predicting the permeability of the compressible tailings thickening bed structure. It is necessary to develop a suitable theoretical permeability model based on the micro-structural parameters of the compressible tailings thickening bed so that it can accurately describe the fluid flow in the compressible tailing thickening bed structure and calculate the permeability of the compressible tailings thickening bed more accurately.

Table 1 Summary of permeability K for different particles porous media.

Reference	Permeability(K) equation	Media
Bourbie et al. [11]	$C\phi^n {d_p}^2$	Porous media
Pape et al. [15]	$\frac{\phi {d_p}^2}{2\tau^2}\left(\frac{2\phi}{3\tau^2(1-\phi)}\right)^{2/(D_f-1)}$	Sandstone
Jeong [18]	$D^2\exp\left(0.709\ln\left(\frac{\phi^{11/3}}{(1-\phi)^2}\right)-5.09\right)$	Particulate porous media
Panda and Lake [16]	$\frac{\phi^3 {d_p}^2}{72\tau(1-\phi)^2}\frac{\left(\gamma C_d^3+3C_d^2+1\right)^2}{\left(1+C_d^2\right)^2}$	Particulate porous media
Civan [12]	$\sqrt{\frac{K}{\phi}}=\alpha\left(\frac{\phi}{1-\phi}\right)^{\beta}$	Porous media
Bayles et al. [17]	$\frac{C\phi^{2+n}}{(1-\phi)^2}$	Fine particle filter cakes
Dai et al. [20]	$C_k S_m^{\frac{3+D_{Tm}}{4-D_{Tm}}}\lambda_{\max}^2\phi^{\frac{(4+D_{Tm})(6-D_{Tt})-3D_{Tt}}{(3-D_{Tt})(4-D_{Tm})}}$	Tight mixed rocks
Xu and Yu [13]	$\frac{(\pi D_f)^{\frac{1-D_T}{2}}\left(4(2-D_f)\right)^{\frac{1+D_T}{2}}}{128(3+D_T-D_f)}\left(\frac{\phi}{1-\phi}\right)^{\frac{1+D_T}{2}}\lambda_{\max}^2$	Porous media
KC equation [10]	$\frac{\phi^3}{36k(1-\phi)^2}d_p^2$	Porous media
Tang and McDonough [19]	$\frac{4{b_1}^2\phi^2}{\left(\sqrt{{c_1}^2\phi^4+4a_1b_1(1-\phi^2)}-c_1\phi^2\right)^2}$	Porous media

The calculation methods of permeability of porous media are mainly divided into the following three types: physical experiment, numerical simulation, and theoretical model construction [21,22]. Physical experiments have high requirements for the preparation of experimental samples and the strength of the pore structure of porous media. It is necessary to ensure that the porosity and pore structure of porous media does not change during the infiltration process, and the cost of the experiment is high. Based on the pore network model (PNM) and the lattice-Boltzmann method (LBM), the calculation of the permeability of complex porous media has been successfully implemented and verified by physical experiments, showing that the use of the method is realistic and reliable [22,23]. In previous research, there have been few studies on the structure and permeability of compressible thickening bed formed by tailings particles. The main reason for the lack of studies is the difficulty in obtaining the pore structure of the compressible tailings thickening bed.

After the tailings slurry is mixed with the flocculant solution, the tailings particles and the flocculant chain undergo adsorption and bridging, netting and sweeping, and electrical neutralization, forming a tailings floc structure and settling to the bottom of the thickener [24–27]. The floc structures settled at the bottom are connected to form the tailings thickening bed interface, and then compression settlement occurs under the gravity of the particles, the pressure of the tailings thickening bed, and the shearing action of the rake [28,29]. Water in the pore space is discharged over the compressible tailings thickening bed by extrusion [25,31], which increases the tailings thickening bed slurry concentration and eventually forms a non-homogeneous, compressible tailing thickening bed structure with high porosity. The low structural strength of the tailings thickening bed increases the difficulty of preparing experimental samples, and the tailings thickening bed structure is in the process of dynamic evolution, making it challenging to obtain the three-dimensional structural morphology of the compressible tailings thickening bed pores accurately and effectively by conventional means. Computed tomography (CT) technology has the characteristics of high efficiency, accuracy, and non-destructiveness. It has been successfully applied to micro-structure studies in rock engineering [30], mining engineering [1,31], geological engineering [32], and other related fields for nondestructive characterization and model construction of pore structures and rock structures.

Inspired by the above research, we conducted non-destructive in-situ sampling of the

compressible tailings thickening bed formed by multi-scale tailings particle size in this study. We used CT technology to obtain the microscopic structure of the compressible tailings thickening bed at different tailings thickening bed pressures with and without shear conditions. Firstly, the 3D pore structure in the compressible tailings thickening bed was constructed by the PNM model. Secondly, compressible tailings thickening bed permeability simulation experiments under different experimental conditions were carried out to obtain the permeability of tailings thickening bed at various pressures. Finally, based on the PNM model, a new theoretical permeability model was constructed using the value of *Tw*, which is the ratio of the length of the throat structure to the equivalent diameter. The simulation results of the permeability of the compressible tailings thickening bed were then compared with the new model's calculated results. The new model and the new model and reliability and accuracy of the new model were verified. This research is expected to provide research ideas for an in-depth understanding of the evolutionary laws of the structure of non-homogeneous porous media and the transport behavior of fluids in complex pore structures. Moreover, a theoretical permeability model based on the throat structure parameters has been developed, providing a reference for calculating permeability in compressible tailings thickening beds.

2. Materials and Methods

2.1 Experimental materials

In this experiment, we employed full tailings from an iron mine in Hebei with a density of 2.749 $g \cdot cm^{-3}$. The particle size distribution (PSD) was determined from a laser granularity analyzer (MS3 000, Malvern, England), and the results are shown in Fig. 1. The specific surface area of the full tailings was 331.4 $m^2 \cdot kg^{-1}$.

The proportion of particles with a diameter less than 20 μm in the tailings was more than 60%, indicating that the tailings are fine-grained. The tailing sand inhomogeneity coefficient *Cu* was 8.32, and the curvature coefficient *Cc* was 1.04. The chemical elements and content in the unclassified tailings were measured by an energy dispersive spectrometer (EDAX TEAM, EDAX, America), and the results are displayed in Fig. 2 and Table 2.

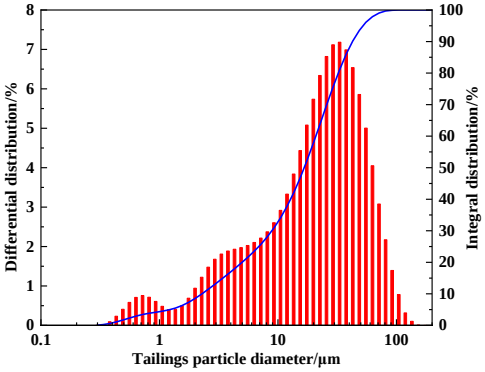

Fig. 1. Tailings particle size distribution curve

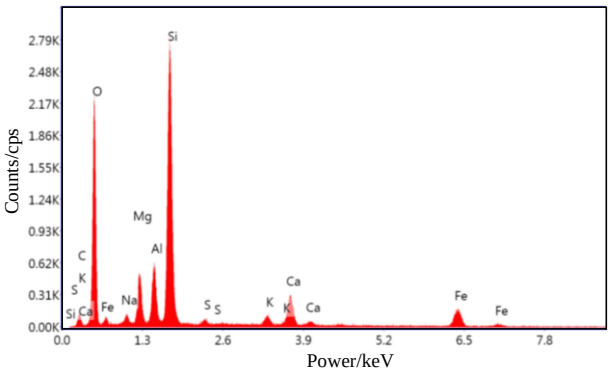

Fig. 2. Tailings energy spectrum

Table 2 Chemical element analysis results of tailings.

Element	C	O	Na	Mg	Al	Si	S	K	Ca	Fe
Content (wt%)	7.85	47.32	1.35	4.41	4.77	21.63	0.37	1.11	4.44	6.75

2.2 Sample preparation and CT scanning

The compressible tailings thickening bed structure is weak and susceptible to deformation when subjected to stress [33]. To ensure that there is no prominent settlement of the thickening bed structure during the CT scanning process, we carried out the static settling experiment of the measuring cylinder indoors to investigate the variation of the interface height of the tailings thickening bed with the settling time, as shown in Fig.3. The results show that the settling law of the tailings thickening bed interface tends to be consistent with different flocculant dosages. After the settling time of 3600 s, the height of the tailings thickening bed interface no longer changed significantly, indicating that the structure of the compressible tailings thickening bed had reached a stable state. Therefore, in this study, we performed a CT scan on the compressible thickening bed structure of tailings with a flocculant dosage of 30 g/t and a settling time of 1 h.

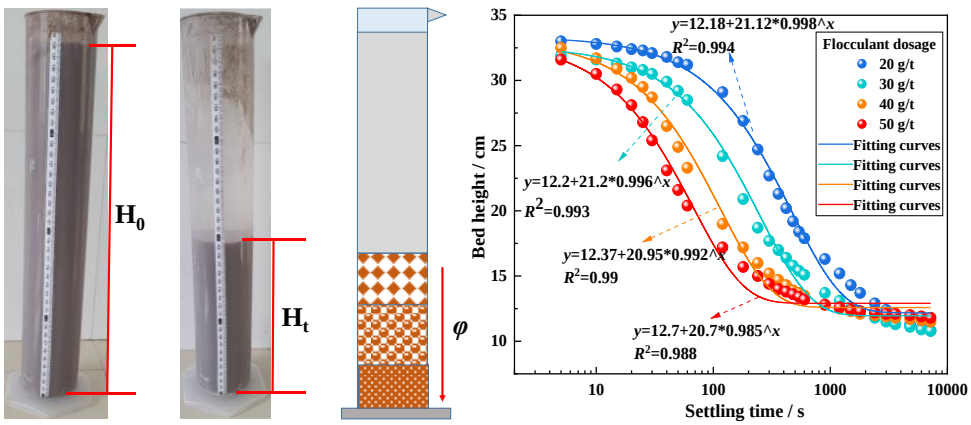

(a) (b)

Fig. 3. Flocculation settling experiment: (a) Flocculation settling experiment process of tailings; (b) The variation of thickening bed interface height with settling time.

In CT scanning experiments, the resolution of the scanned sample is closely related to the size of the scanned sample. When the size of the scanned sample is large, high resolution cannot be obtained, resulting in some compressible tailings thickening bed structure information being hidden. When the size of the scanned sample is small, although high resolution can be obtained, the friction force of the sampling tube wall will cause severe damage to the compressible tailings thickening bed structure. We conducted many pre-experiments before the formal CT scanning experiment of the compressible tailings thickening bed structure. Finally, we selected the sampling tube diameter of 2.1 cm and the sampling height of 2 cm as the structural size of the scanned sample. The sampling height of the compressible tailings thickening bed structure with and without shear, as shown in Table 3, and the number of scanned samples under each experimental condition is 8.

Table 3 Sampling heights of experimental samples.

0 rpm-1 h								
Thickening bed height (cm)	28	22	12	10	8	6	4	2
1 rpm-1 h								
Thickening bed height (cm)	24	22	12	10	8	6	4	2

The sampled samples were transmitted directly into the experimental platform for scanning. The high-resolution CT apparatus (FF35, YXLON, Germany) was used for the experiment. After pre-experimental debugging, the best scanning effect can be achieved when the scanning voltage is 100 KV and the scanning current is 200 μA. The voxel resolution of this sample scan is 12.9 μm, and each image's pixels are 2146 * 2146. Due to the hardening impact of the scanning beam, avoiding distortion and artifacts in the scanned images, mathematical algorithms such as median filtering was used during the scanning process to make the corresponding corrections [34]. Fig. 4 shows the whole CT scanning experiment and data processing process.

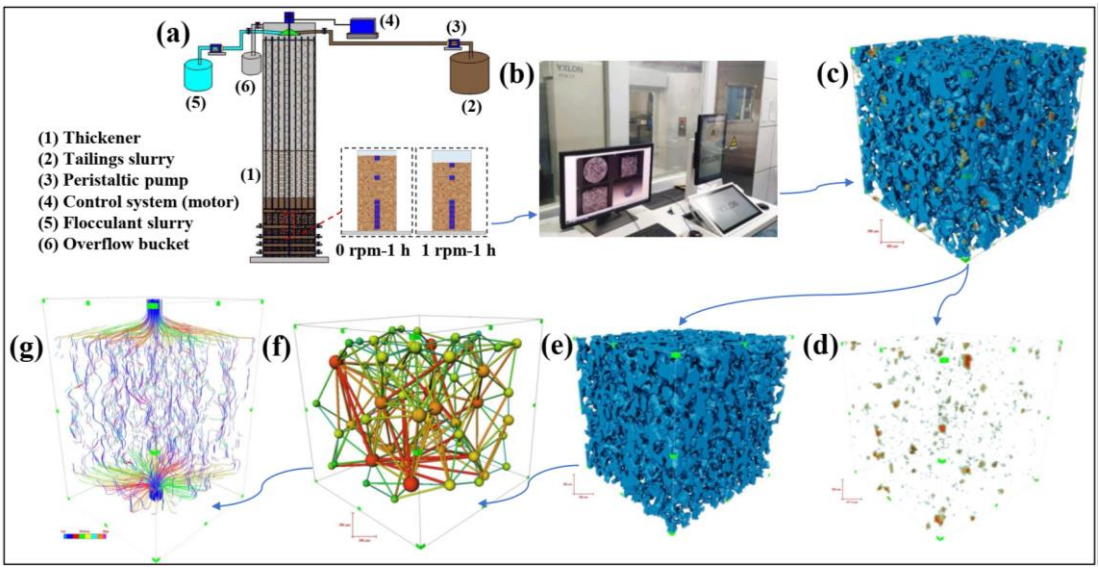

Fig. 4. CT scanning experiment: (a) Sampling preparation; (b) CT scanning; (c) Pore structure; (d) Isolated pores; (e) Connecting pores; (f) PNM model; (g) Seepage path.

2.3 Absolute permeability experiment simulation

The permeability simulation of the compressible tailings thickening bed structure was carried out based on the XLab Extension module of Avizo software [23]. The seepage path of the fluid inside tailings thickening bed structure and the permeability can be obtained by giving a particular value of pressure in the direction of fluid transport. The absolute permeability simulation of the compressible tailings thickening bed structure was performed using the Native-Stokes equation as in Eq. (1).

$$\begin{cases} \vec{\nabla}.\vec{V} = 0 \\ \mu\nabla^2\vec{V} - \vec{\nabla}P = \vec{0} \end{cases} \tag{1}$$

where $\vec{\nabla}.$ is the divergence operator, $\vec{\nabla}$ is the gradient operator, $\vec{V}$ is the velocity of the fluid, μ is the dynamic viscosity of the flowing fluid, ∇^2 is the Laplacian operator, and P is the pressure of the liquid.

For incompressible fluids, the permeability of the compressible tailings thickening bed structure can be calculated using Darcy's law.

$$K = -\mu\frac{\langle u_z \rangle}{\Delta P} \tag{2}$$

where $\langle u_z \rangle$ is the overall mean value of velocity in the z-direction, ΔP is the pressure difference between the outlet and inlet of the compressible tailings thickening bed.

The pressure of the compressible tailings thickening bed increases with the decrease in the thickening bed height, and the fluid inside the thickening bed flows from the bottom to the top of the thickening bed under the pressure gradient. We obtained the pressure values at the top and bottom of the tailings thickening bed at different heights according to the concentration of the tailings thickening bed and its height, as shown in Eq. (3). The calculated inlet and outlet pressures of the tailings thickening bed are input into the simulation software.

$$P_i = \sum_i^n \left(\frac{2.749 g h_i}{2.749 - 1.749 \omega_i} \right) \tag{3}$$

where h_i is the height of the i section of the compressible tailings thickening bed, ω_i is the concentration of the i section of the compressible tailings thickening bed.

The simulation process continues until the steady state and the convergence criterion is:

$$\text{error} = \frac{k_{old} - k_{new}}{k_{old}} < 10^{-5} \tag{4}$$

2.4 The pore network modelling

The threshold segmentation of CT images directly affects the subsequent extraction of the compressible tailings thickening bed pore structure. Accurate threshold segmentation technology provides a theoretical basis for the quantitative characterization of data and plays a significant role in the quantitative analysis of data. Considering that there are only solid-liquid two-phase substances in the experimental samples, this study uses the Otsu algorithm as the theoretical support for the threshold segmentation of this image [35].

After completing the extraction of the pore structure of the compressible tailings thickening bed, a 3D model of the pore structure was constructed, and a PNM model of the pore structure was constructed by the maximum sphere algorithm [22,31]. The maximum sphere radius R is defined as follows:

$$R_{Right}^2 = dist^2\left(C, V_g\right) = \left(x_1 - x_g\right)^2 + \left(y_1 - y_g\right)^2 + \left(z_1 - z_g\right)^2, C \in S, V_g \in S_g \tag{5}$$

$$R_{Left}^2 = \max\left\{ dist^2\left(V, C\right) \middle| dist^2\left(V, C\right) < R_{Right}^2, C \in S, V \in S \right\} \tag{6}$$

$$R_{Left}^2 \le R^2 < R_{Right}^2 \tag{7}$$

where S and S_g represent the pore and solid space, respectively. R_{Right}^2 denotes the square of the

distance from the sphere center C (x_1, y_1, z_1) to the closest grain voxel V_g (x_g, y_g, z_g). R_{Left}^2 denotes the maximum distance from the sphere center of a void voxel V (x, y, z) that exists in the R_{Right} sphere.

Based on the PNM model, the parameter information of pore structure and throat structure can be obtained, as shown in Table 4.

Table 4 Interpretations of 3D micro-structural parameters.

Parameter	Symbol	Definition	Explanation
Pore Eqdiameter	D_p	$D_p = \left(6V_{3D}/\pi\right)^{1/3}$	V_{3D} represents the volume of an individual pore.
Throat Eqdiameter	D_c	$D_c = \left(4A/\pi\right)^{1/2}$	A is the contact area between two connected pores. It is the narrowest region between pores.
Channel Length	L_c	$L_c = \sqrt{(\Delta x)^2 + (\Delta y)^2 + (\Delta z)^2} - R_1 - R_2$	R_1 and R_2 represent the radius of the connected pores, respectively. Δx, Δy, and Δz represent the coordinate difference of the connected pores.
Porosity	ϕ	$\phi = V_v / V_t$	V_v and V_t represent the drainage channels volume and the total volume of the samples, respectively.
Connectivity	φ_c	$\varphi_c = V_c / V_v$	V_v and V_c represent the drainage channels volume and the connectivity volume of the drainage channels, respectively.

2.5 Propose a new permeability model

Another objective of this study is to construct a new model to characterize the permeability of compressible tailings thickening beds. The PNM model divides the pore structure in the tailings thickening bed into the spherical pore and stick throat structures [1,31]. The stick throat structure connects the spherical pore structures for fluid transfer between adjacent spherical pore structures [14]. Moreover, during the compression of the tailings thickening bed structure, the fluid in the thickening bed is also discharged above the thickening bed interface through the throat structure [31]. Therefore, the throat structure becomes a key parameter for the seepage phenomenon in the compressible tailings thickening bed structure. Considering the compression process of the tailings thickening bed structure, the length and equivalent diameter of the throat structure are changed. In

this study, a dimensionless parameter T_w was proposed to characterize the trend of throat structure during tailings thickening bed compression. Fig. 5 shows the equivalent schematic diagrams of the spherical pore structure and the stick throat structure in the compressible tailings thickening bed, as well as the morphology of the throat structure at different values of T_w.

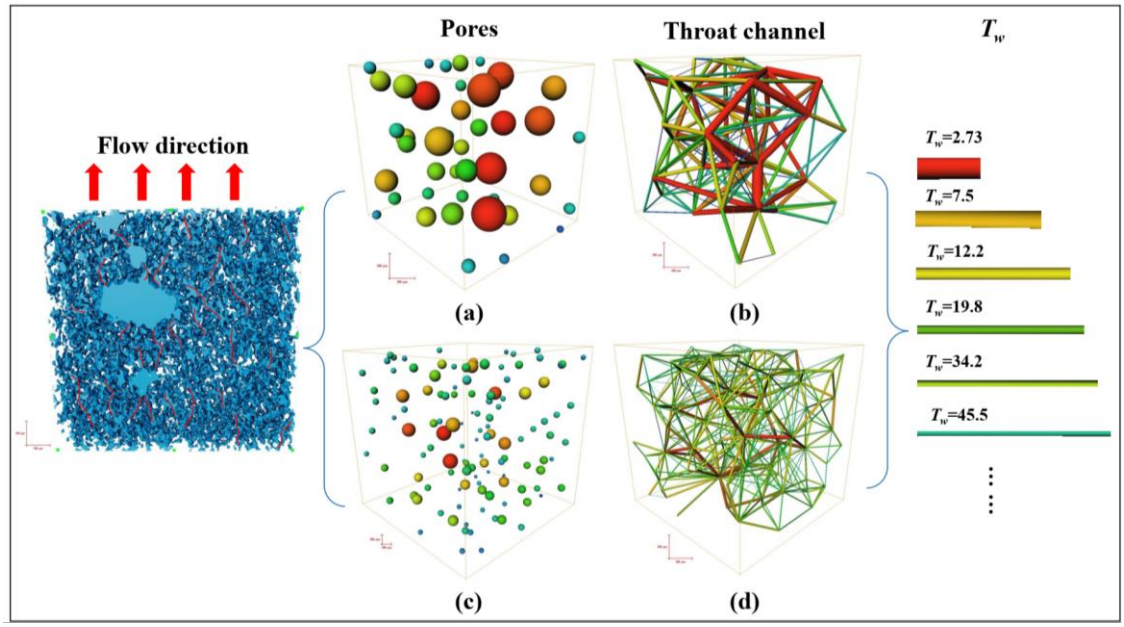

Fig. 5. Classification of pore structure in compressible tailings thickening bed: (a) Pores (0 rpm-1 h); (b) Throat (0 rpm-1 h); (c) Pores (1 rpm-1 h); (d) Throat (1 rpm-1 h).

The definition of throat structure parameter T_w is shown in Eq. (8).

$$T_w = \frac{L_c}{D_c} \tag{8}$$

where L_c is the channel length of the throat, D_c is the equal diameter of the throat.

The construction of the new model in this study is proposed based on the throat structure parameters of the PNM model of the compressible tailings thickening bed pore structure. The cross-sectional area of the tailings thickening bed is composed of the area of connected pores along the Z-axis, the area of isolated pores, and the area of tailings particles:

$$A_t = A_{pc} + A_{pi} + A_s \tag{9}$$

where A_t is the cross-sectional area, A_{pc} is the total area of the throat on the cross-section, A_{pi} is the total area of the throat on the cross-section, A_s is the total area of tailings particles in the cross-section.

Assuming that the area of pores connected in the cross-section of the tailings thickening bed

is composed of throat structures, the total area and average diameter of the throats connected in each cross-section can be expressed as:

$$A_{pc} = \sum_{i}^{n} \pi D_i^2 / 4 = n\pi D_{ave}^2 / 4 \tag{10}$$

where D_i is the diameter of the ith throat, D_{ave} is the average throat diameter.

The relationship between the area of the connected throat on the cross-section of the tailings thickening bed and the cross-sectional area of the tailings thickening bed as shown in Eq. (11) [36]:

$$A_t \phi \varphi_c = nA_{ave} \tag{11}$$

where A_{ave} is the average throat area, φ_c is pore connectivity.

The total volume of the tailings thickening bed and the volume of the connected pores in the tailings thickening bed can be expressed by equations (12) and (13):

$$V_t = A_t L_s \tag{12}$$

$$V_{pc} = \sum_{i}^{n} A_i L_i = nA_{ave} L_{ave} = V_t \phi \varphi_c \tag{13}$$

where V_t is the total volume of the tailings thickening bed, L_s is the height of the tailings thickening bed, V_{pc} is the volume of the connected pores, A_i is the diameter of the ith throat, L_i is the length of the ith throat, L_{ave} is the average length of throat.

Considering that the fluid in the compressible tailings thickening bed structure is an incompressible Newtonian fluid, the flow rate of the compressible tailings thickening bed can be expressed by Darcy's law [37]:

$$Q = \frac{KA_t \Delta P}{\mu L_s} \tag{14}$$

where Q is the flow through the compressible tailings thickening bed, K is the permeability, $\triangle P$ is the pressure difference, μ is the viscosity of the fluid.

Based on the cylindrical structure of the throat, the fluid flow through a single throat can be characterized using the Hagen-Poiseuille [38]:

$$q_i = \frac{\pi D_i^4 \Delta P}{128 \mu L_i} \tag{15}$$

There are *n* throats on each section along the Z-axis of the tailings thickening bed. The total flow of throats on each section can be expressed as:

$$Q = \sum_{i}^{n} \frac{\pi D_i^4 \Delta P}{128 \mu L_i} = n \frac{\pi D_{ave}^4 \Delta P}{128 \mu L_{ave}} \tag{16}$$

Inserting Eqs. (11) and Eq. (14) into Eq. (16), we can obtain the relationship between pore throat equivalent diameter and permeability, as shown in Eq. (17):

$$D_{ave} = 2\sqrt{\frac{A_{ave}}{\pi}} = \frac{4\sqrt{2KL_{ave}}}{\sqrt{\phi \phi_c L_s}} \tag{17}$$

Inserting Eq. (8) into Eq. (17), we finally obtain a new permeability model, as shown in Eq. (18):

$$K = \frac{\phi \varphi_c D_{ave} L_s}{32 T_{wave}} \tag{18}$$

where T_{wave} is the average throat T_w value.

3. Results and discussion

3.1 The variation in tailings thickening bed concentration and pressure

From Fig. 6, we can see that the tailings thickening bed's pressure decreases linearly with the interface height with and without shear. Under pressure and rake shear, the fluid in the tailings thickening bed discharged to the top of the tailings thickening bed interface, which increases the concentration of the tailings thickening bed. The tailings thickening bed concentration decreases with the increase in the tailings thickening bed height, indicating that the tailings thickening bed structure inside the deep cone thickener is a non-homogeneous porous medium. In comparing tailings thickening bed concentrations with and without shear, it was found that the concentration with shear was higher than that without shear. The main reason is that the rake's forced shearing action drives the fluid's discharge in the tailings thickening bed, which is consistent with the findings of previous studies [28,31].

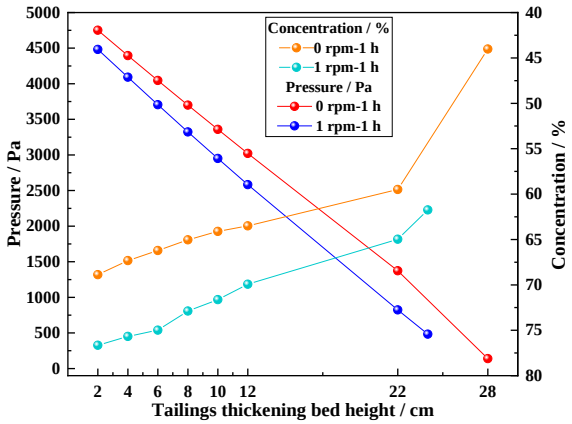

Fig. 6. Variation of concentration and pressure with tailings thickening bed height.

3.2 Representative elementary volume

In general, the raw data after CT scanning is large and contains many pore structure parameters inside the tailings thickening bed, which also requires more computational resources and storage space during the processing and simulation of the data. Therefore, we use the concept of representative cell volume to obtain the smallest volume that can represent the structural characteristics of the entire tailings thickening bed pore structure [32,39]. We set up nine sampling points for each raw data set to reduce the data error. One is located in the center of the raw data, and the remaining eight sampling points are evenly distributed around the center sampling point, as shown in Fig. 7.

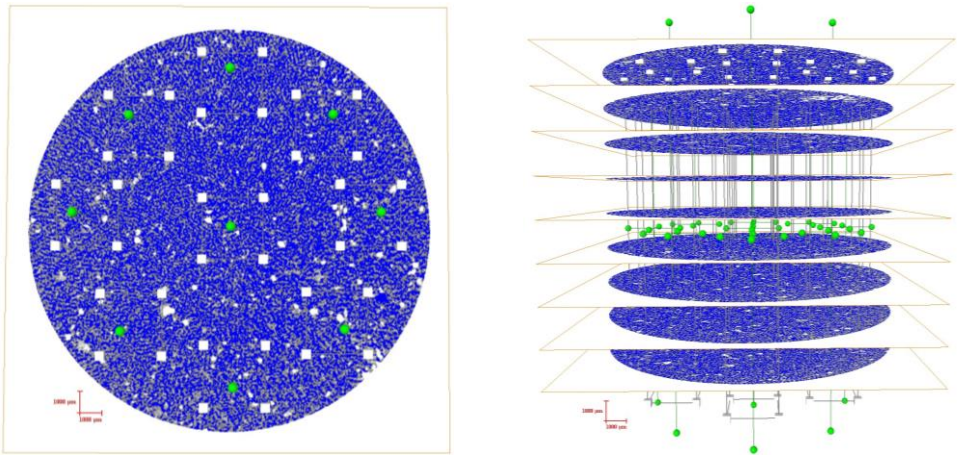

(a) (b)

Fig. 7. REV analysis diagram: (a) REV sampling position distribution; (b) REV sampling view.

We took a cube with a side length of 400 μm as a starting point and obtained the trends of the compressible tailings thickening bed porosity with cube size at different tailings thickening bed pressures, as shown in Fig. 8(a) and Fig. 8(b). The data show that the volatility of porosity is also more significant for smaller cube sizes, which is unsuitable for REV. As the cube size increases, the volatility of porosity gradually decreases, and the porosity remains stable when the cube side

length increases to 1500 μm. Therefore, the final REV is chosen as 1500 μm × 1500 μm × 1500 μm.

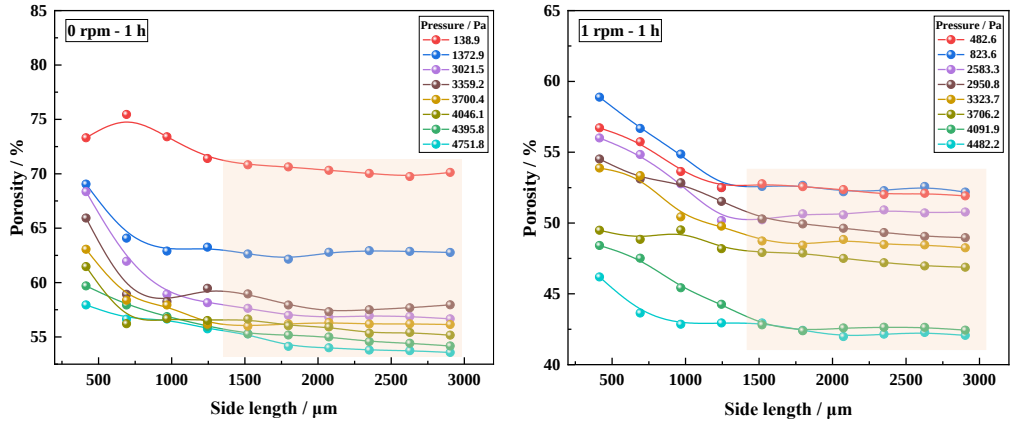

(a) (b)

Fig. 8. Calculation of REV porosity: (a) 0 rpm-1 h; (b) 1 rpm-1 h.

3.3 PNM reconstruction and quantitative characterization of pore structure

Based on the selected REV, we obtain the pore structure of the compressible tailings thickening bed by threshold segmentation, perform 3D reconstruction and target value segmentation on the pore structure, and obtain the PNM model of the pore structure by the maximum ball algorithm [22,31]. Limited by the article's length, this study presents three tailings thickening bed structures at different tailings thickening bed pressures with or without shear conditions, as shown in Fig. 9 and Fig. 10.

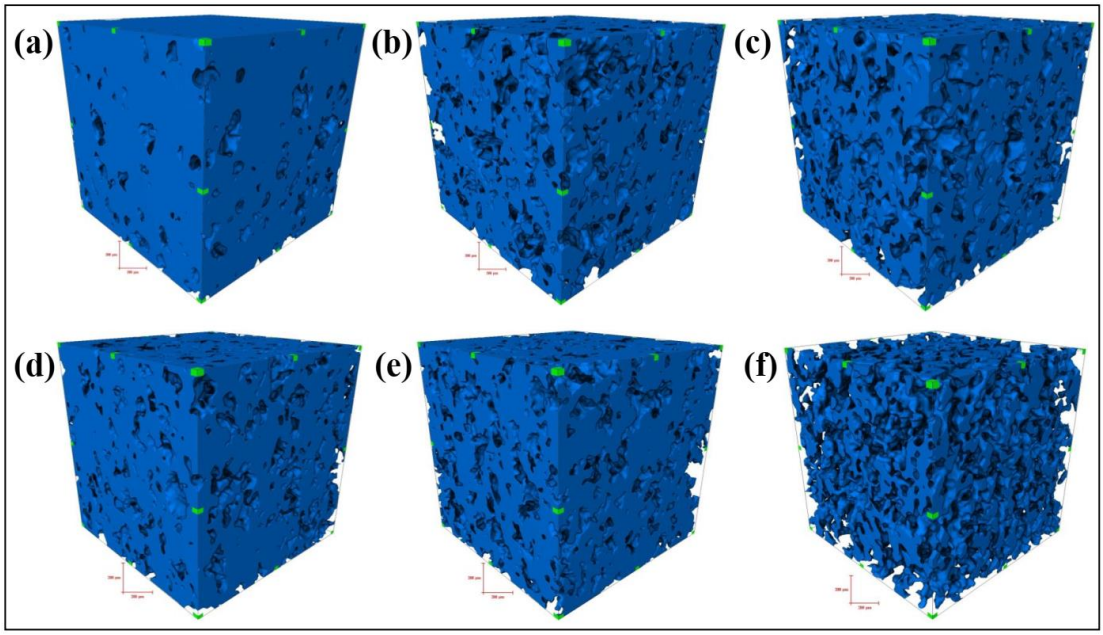

Fig. 9. 3D pore structure of compressible tailings thickening bed: (a) 0 rpm-1 h-138.9 Pa; (b) 0 rpm-1 h-1372.9 Pa; (c) 0 rpm-1 h-4751.8 Pa; (d) 1 rpm-1 h-482.6 Pa; (e) 1 rpm-1 h-823.6 Pa; (f) 1 rpm-1 h-4482.2 Pa.

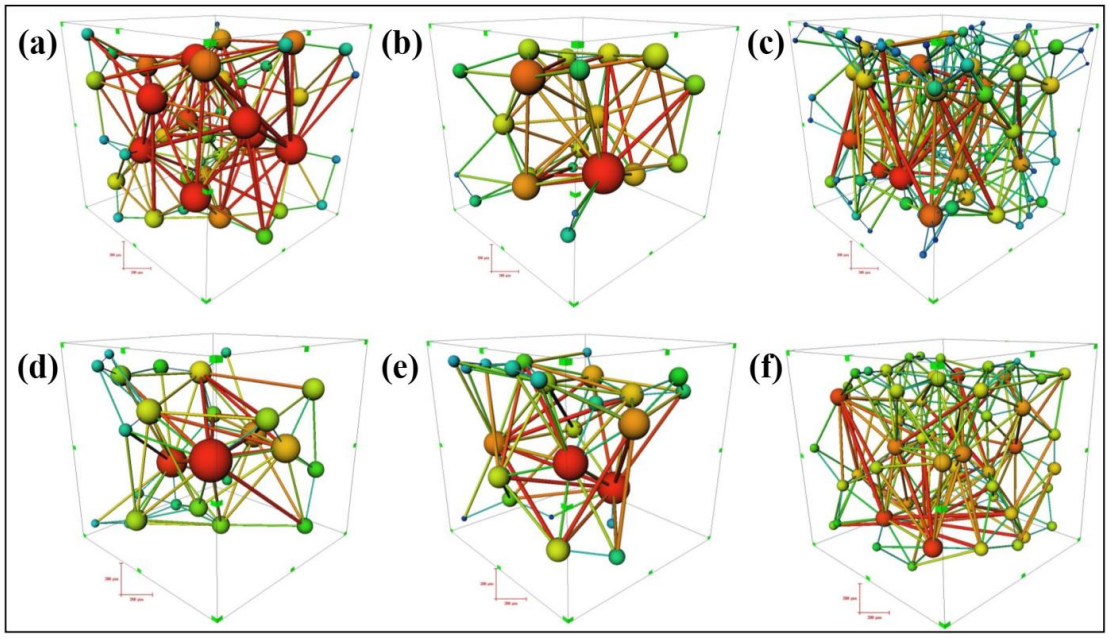

Fig. 10. PNM model of compressible tailings thickening bed pores: (a) 0 rpm-1 h-138.9 Pa; (b) 0 rpm-1 h-1372.9 Pa; (c) 0 rpm-1 h-4751.8 Pa; (d) 1 rpm-1 h-482.6 Pa; (e) 1 rpm-1 h-823.6 Pa; (f) 1 rpm-1 h-4482.2 Pa.

Fig. 11 shows the variation of compressible tailings thickening bed porosity and pore connectivity at different tailings thickening bed pressures with and without shear. The data show that the porosity of the compressible tailings thickening bed structure decreases with the increase in the tailings thickening bed pressure. The porosity of the tailings thickening bed structure gradually decreased from 64.6% to 45.5% without shear. After shearing, the porosity of the tailings thickening bed structure was gradually reduced from 51.8% to 29.5%. The pores of the tailings thickening bed maintain high connectivity, indicating that the fluid has high transport in the tailings thickening bed structure. However, as the pressure of the tailings thickening bed increased, the pore connectivity decreased to different degrees. The pore connectivity gradually decreased from 99.9% to 99.76% without shear. After shearing, the pore connectivity gradually decreased from 99.64% at the top to 97.22% at the bottom.

The results of the above data show that the porosity and connectivity of the compressible tailings thickening bed with shear are lower than those without shear. The analysis found that the strength of the compressible tailings thickening bed structure was low, and the pore volume completed iso-volume exchange with the tailings particles under the action of tailings thickening bed pressure, which realized the transformation of the compressible tailings thickening bed slurry from low concentration to high concentration. The rake shear caused forced damage to the pore

structure, promoted the equal volume exchange between the pore structure and tailings particles, and increased the concentration of the tailings thickening bed slurry while reducing the porosity of the tailings thickening bed structure, which is consistent with the findings in section 3.1. At the same time, the tailings thicken the bed structure in the compression process, and the tailings particles on the pore structure plugging effect, transforming partially connected pores to isolated pores. With the increase of the tailings thickening bed pressure, the plugging effect of particles also strengthened [40,41]. The shearing action of the rake forces the azimuthal angle of the tailings particles to change, intensifying the degree of transformation of the connected pore structure to isolated pores, resulting in lower pore connectivity with shear than without shear [41]. Additionally, the shearing action of the rake resulted in a significant reduction in the permeability of the compressible tailings thickening bed structure, which we will further investigate in Section 3.4.

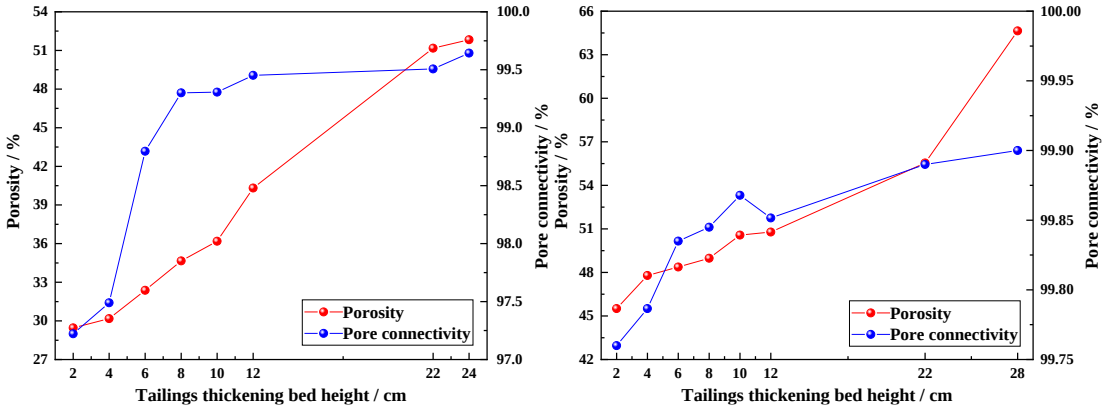

Fig. 11. Variation of porosity and connectivity of the compressible tailings thickening bed structure with the height :(a) 0 rpm-1 h; (b) 1 rpm-1 h.

Based on the PNM model of the compressible tailings thickening bed pore structure, we obtained the distribution of the 3D equivalent diameter of the spherical pore structure in the PNM model, as shown in Fig. 12. The data fitting results show that the spherical pore diameters of the compressible tailings thickening bed conform to the gamma distribution [32]:

$$f(x)=\frac{1}{b^{a}\int_{0}^{\infty}t^{a-1}\exp(-t)\,dt}x^{a-1}\exp(-x/b) \qquad (20)$$

where a and b are the function coefficients of the Gamma distribution.

From Fig. 12(a), we can see that the distribution range of spherical pore diameters decreases with the increase in the tailings thickening bed pressure without shear. The distribution range of

spherical pore diameter decreased from 55.2 μm~740.4 μm to 54.1 μm~503.6 μm when the tailings thickening bed pressure increased from 138.9 Pa to 1372.9 Pa. The distribution of the spherical pore diameter was concentrated between 31.2 μm and 383.9 μm when the tailings thickening bed pressure was between 3021.5 Pa and 4751.8 Pa. It did not decrease significantly with the increase in the tailings thickening bed pressure, which indicates that the spherical pore structure of the compressible tailings thickening bed has reached a relatively stable state at the tailings thickening bed pressure of 3021.5 Pa without shear. The distribution range of the spherical pore diameter of the compressible tailings thickening bed with shear is consistent with that without shear, as shown in Fig.12 (b). The distribution of spherical pore diameters decreased from 80.2 μm ~ 585.2 μm to 37.9 μm ~ 399.9 μm when the pressure increased from 482.6 Pa to 823.6 Pa at the rake speed of 1 rpm. The distribution of spherical pore diameter was concentrated between 27.2 μm and 257.9 μm when the pressure ranged from 2583.3 Pa to 4482.2 Pa. Moreover, the spherical pore structure with shear reached a relatively stable state when the pressure exceeded 2583.3 Pa.

The results show that the distribution range of spherical pore diameters with shear is smaller than without shear. The data indicates that the shearing action not only promotes the transformation of the large pore structure to the small pore structure in the compressible tailings thickening bed but also reduces the pressure required for the spherical pore structure to reach the stable state, which accelerates the transformation rate of the pore structure of the compressible tailings thickening bed from the unstable state to the stable state.

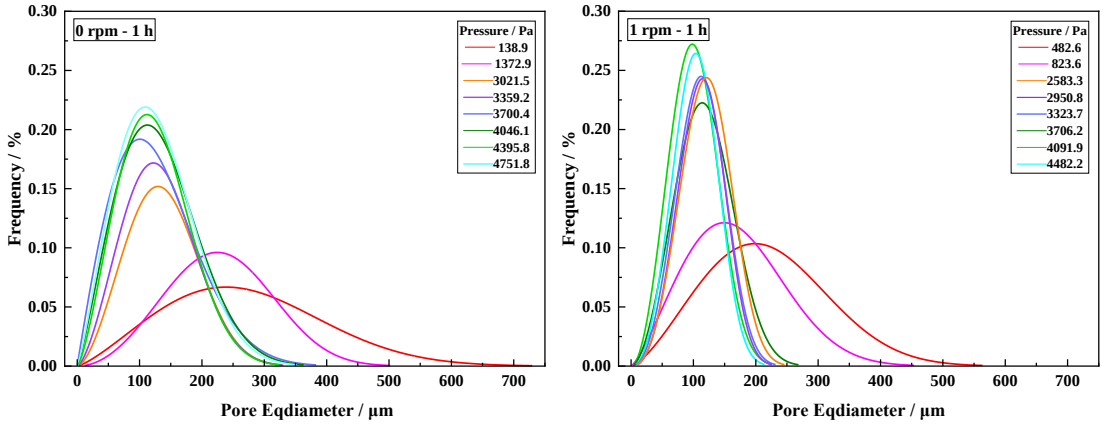

(a) (b)

Fig. 12. Variation of spherical pore diameter distribution with pressure: (a) 0 rpm-1 h; (b) 1 rpm-1 h.

In the PNM model of the compressible tailings thickening bed pore structure, the stick throat structure connects the spherical pore structure, facilitating the flow and discharge of fluids in the

tailings thickening bed. Related studies have shown that the fluid in the compressible tailings thickening bed structure discharged through the throat structure to the top of the tailings thickening bed interface, and the throat structure plays an essential role in the permeation of the compressible tailings thickening bed structure. Fig. 13 shows the variation in the throat diameter distribution with the tailings thickening bed pressure, and the fitting results of the data show that the throat diameters all obeyed the Weibull distribution [32]:

$$f\left(x\right)=\frac{\alpha}{\beta^{\alpha}}x^{\alpha-1}\exp\left(-\left(x/\beta\right)^{\alpha}\right) \tag{21}$$

where α and β are the function coefficients of the Weibull distribution.

From Fig. 13(a) and Fig. 13(b), we can find that the distribution of stick throat diameters changes in the same pattern with and without shear, and both decrease with increasing tailings thickening bed pressure. When without shear, the distribution of throat diameter ranged from 2.85 μm to 495.2 μm when the tailings thickening bed pressure was between 138.9 Pa and 1372.9 Pa. The throat structure reached a relatively stable state when the tailings thickening bed pressure was between 3021.5 Pa and 4751.8 Pa, and the throat diameter concentrated in the 2.85 μm to 220.7 μm range. When with shear, the distribution of throat diameter ranged from 2.85 μm to 476.8 μm when the tailings thickening bed pressure was between 482.6 Pa and 823.6 Pa. The throat structure reached a relatively stable state when the tailings thickening bed pressure was between 2583.3 Pa and 4482.2 Pa, and the throat diameter concentrated in the range of 2.85 μm~165.8 μm. Compared with the distribution range of throat diameter without shear, the distribution range of throat diameter with shear is small, indicating that rake shearing not only caused damage to the spherical pore structure but also caused damage to the stick throat structure, causing the larger structural throat structure to change to the small throat structure [31,42].

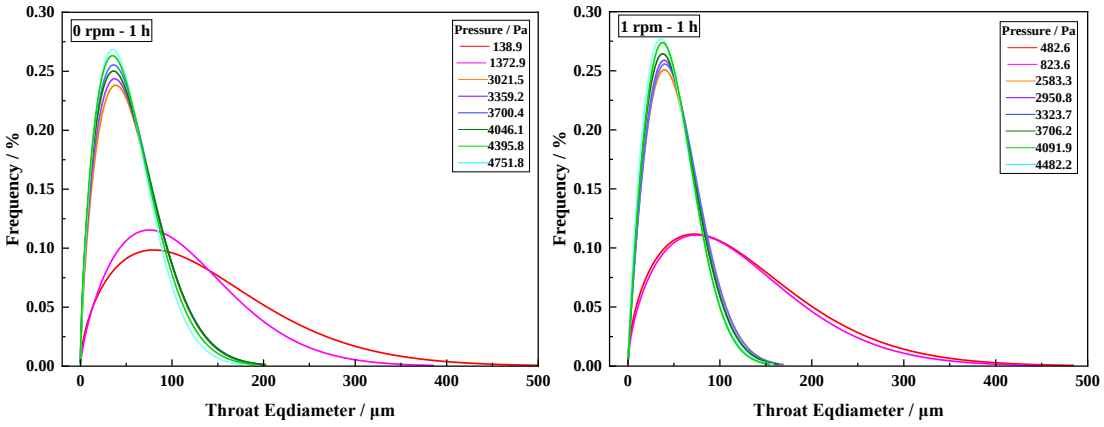

(a) (b)

Fig. 13. Variation of the diameter distribution of the stick throat with pressure: (a) 0 rpm-1 h; (b) 1 rpm-1 h.

Under the action of the tailings thickening bed pressure and rake shear, not only does the diameter of the throat change, but the length of the throat also undergoes changes. From Fig. 14(a) and Fig. 14(b), it can be seen that the length of the throat decreases with the increase in the tailings thickening bed pressure with and without shear. When without shear, the tailings thickening bed pressure increased from 138.9 Pa to 1372.9 Pa, and the main distribution range of throat length decreased from 500 μm~1100 μm to 400 μm~900 μm range. When the tailings thickening bed pressure was between 3021.5 Pa and 4751.8 Pa, the throat length was mainly concentrated in the range of 200 μm~600 μm. Moreover, with the increased tailings thickening bed pressure, the throat length did not decrease significantly, indicating that the throat structure had reached a relatively stable state.

When with shear, the main distribution range of throat length decreased from 450 μm~1000 μm to 400 μm~900 μm as the tailings thickening bed pressure increased from 482.6 Pa to 823.6 Pa. When the tailings thickening bed pressure was between 2583.3 Pa and 4482.2 Pa, the throat length was mainly concentrated in the range of 200 μm~500 μm. And with the increase in tailings thickening bed pressure, the throat length did not change significantly, which indicated that the throat structure had reached a stable state. Compared with the throat length without shear, the throat length was further reduced with shear, indicating that the damage to the throat structure in the compressible tailings thickening bed was more severe by rake shear action.

The throat length plays a vital role in the ease of fluid flow in the compressible tailings thickening bed structure. The more prolonged throat structure increases the resistance to fluid flow. It is not conducive to fluid discharge in the tailings thickening bed to the outside of the tailings thickening bed interface, which is consistent with the mechanism of pore tortuosity [43].

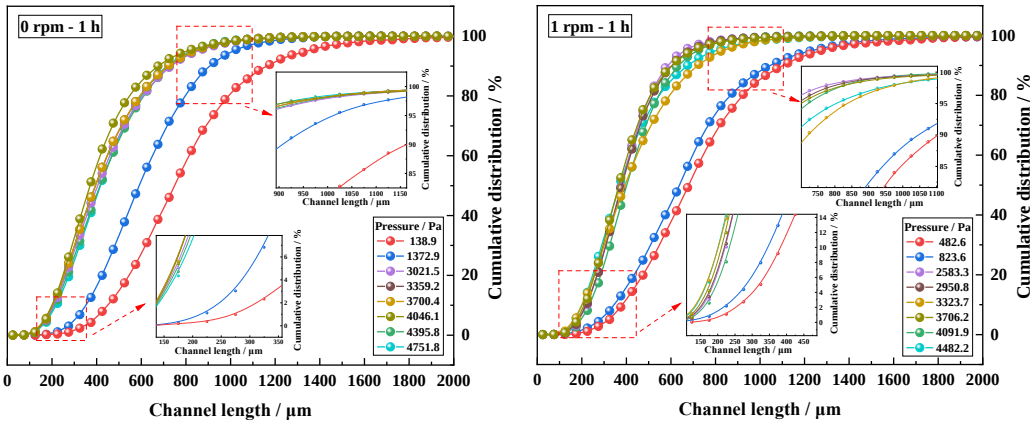

(a) (b)

Fig. 14. Variation of throat length with pressure: (a) 0 rpm-1 h; (b) 1 rpm-1 h.

3.4 Absolute permeability simulation results

The force variations of the compressible tailings thickening bed structure with and without shear and the seepage traces along the Z-axis are presented in Figs. 15 and 16, respectively. Due to the space limitation of the paper, we present the simulation results for three tailings thickening beds with and without shear at different tailings thickening bed pressures, respectively. As shown in Fig. 15, the pressure transfer in the compressible tailings thickening bed occurs mainly in the Z-axis, along the top of the tailings thickening bed toward the bottom, i.e., the bottom of the tailings thickening bed is subjected to the highest pressure. The fluid in the compressible tailings thickening bed is discharged to the top under the pressure difference, increasing the concentration of the tailings thickening bed.

The flow traces of fluid in the compressible tailings thickening bed as shown in Fig. 16. We can see that there are multiple flow traces of fluid in the compressible tailings thickening bed, especially in the top area of the tailings thickening bed, which indicates that the permeability of the top of the tailings thickening bed is high. The fluid can be discharged more quickly. As the pressure of the tailings thickening bed increases, the number of fluid flow traces in the compressible tailings thickening bed gradually decreases, indicating that the fluid flow at the bottom of the tailings thickening bed becomes more complex and is not conducive to the discharge of fluid in the tailings thickening bed.

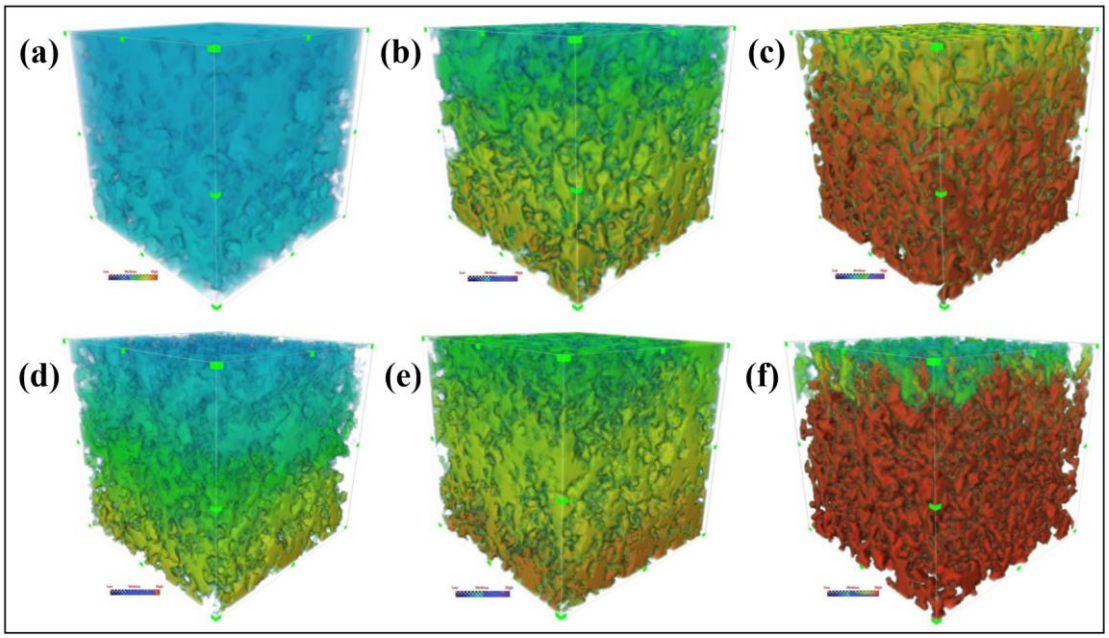

Fig. 15. Distribution of pressure in the pores of the tailings thickening bed: (a) 0 rpm-1 h-138.9 Pa; (b) 0 rpm-1 h-1372.9 Pa; (c) 0 rpm-1 h-4751.8 Pa; (d) 1 rpm-1 h-482.6 Pa; (e) 1 rpm-1 h-823.6 Pa; (f) 1 rpm-1 h-4482.2 Pa.

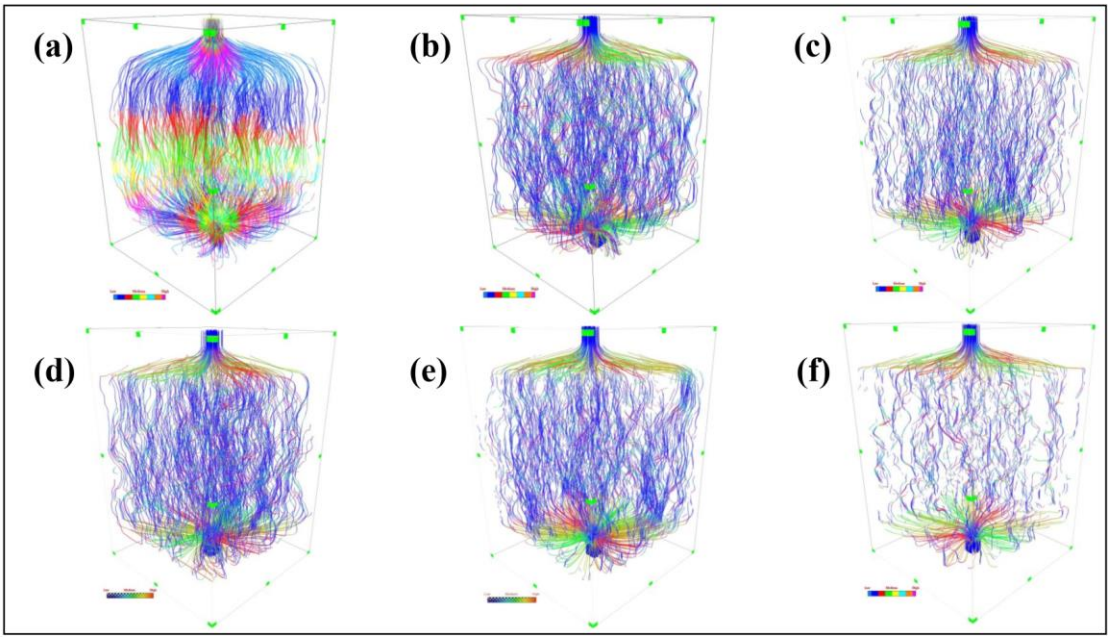

Fig. 16. Distribution of seepage path in tailings thickening bed: (a) 0 rpm-1 h-138.9 Pa; (b) 0 rpm-1 h-1372.9 Pa; (c) 0 rpm-1 h-4751.8 Pa; (d) 1 rpm-1 h-482.6 Pa; (e) 1 rpm-1 h-823.6 Pa; (f) 1 rpm-1 h-4482.2 Pa.

The permeability of the tailings thickening bed decreased with the decrease in the tailings thickening bed height with and without shear, as shown in Fig. 17. The permeability of the tailings thickening bed decreased from 870.36 d at the top to 134.86 d at the bottom without shear, a decrease of 84.5%. The tailings thickening bed permeability decreased from 529.16 d at the top to

80.36 d at the bottom with a shear speed of 1 rpm, a decrease of 84.8%. The data showed that the permeability at the top of the tailings thickening bed was much greater than that at the bottom with and without shear. It indicates that at the top of the tailings thickening bed, the fluid in the tailings thickening bed is more easily discharged through the pore structure of the compressible tailings thickening bed. As the tailings thickening bed height decreases, the decrease in tailings thickening bed permeability also gradually decreases, and the permeability of the tailings thickening bed gradually stabilizes.

We combined the compressible tailings thickening bed permeability results with the tailings thickening bed concentrations at different heights in section 3.1, and it was found that the permeability of the tailings thickening bed decreased with the increase in the tailings thickening bed concentration. The tailings thickening bed permeability tends to stabilize when the tailings thickening bed concentration is between 63.5% and 68.9% without shear. In contrast, the tailings thickening bed permeability tends to stabilize only when the tailings thickening bed concentration is between 69.9% and 76.6% with shear. The results mean that in the actual production process of the mine, a high concentration of tailings thickening bed slurry has been formed at the bottom of the thickener, and its concentration is difficult to be improved again. At the same time, it also indicates that in the thickening process of the mine, it is necessary to consider the appropriate discharge range of the bottom flow concentration for different working conditions to prevent tailings thickening bed slurry slabbing and pressure rake accidents.

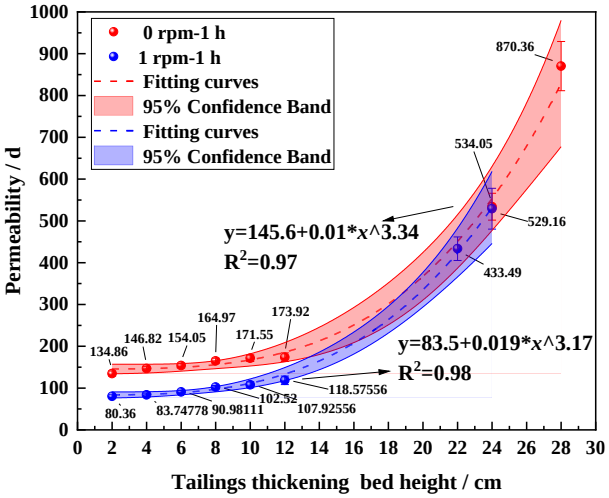

Fig. 17. The permeability of compressible tailings thickening beds varies with height.

3.5 Application and validation of the new model

To assess the reliability of the new model for compressible tailings thickening bed

permeability, we compared the simulation results of the compressible tailings thickening bed permeability with the empirical equations and the permeability predicted by the new model. In choosing empirical models, to make the results of the comparison more convincing, we chose the fractal permeability model without empirical parameters proposed by Xu and Yu [13], as shown in Eq. (22). The Kozeny-Carman (KC) equation with one empirical constant[10], as shown in Eq. (23). The Civan model with two empirical parameters[12], as shown in equation (24).

$$K=\frac{\left(\pi D_f\right)^{\frac{1-D_T}{2}}}{128}\frac{\left(4\left(3-D_f\right)\right)^{\frac{1+D_T}{2}}}{3-D_f+D_T}\left(\frac{\phi}{1-\phi}\right)^{\frac{1+D_T}{2}}\lambda_{\max}^2 \tag{22}$$

where K is the permeability, $2<D_f<3$ is the fractal dimension of the three-dimension pore structure, $1<D_T<2$ is the fractal dimension for tortuosity, ϕ is the porosity of the compressible tailings thickening bed，$\lambda_{\max}$ is the largest diameter of pores.

$$K=\frac{\phi^3}{k\left(1-\phi\right)^2S^2}=\frac{\phi^3}{36k\left(1-\phi\right)^2}d_p^2 \tag{23}$$

where S is specific surface area of particle, k is the KC constant, in this study, the k values were taken as 3.5 and 5, d_p is the mean diameter of tailings particles.

$$\sqrt{\frac{K}{\phi}}=\alpha\left(\frac{\phi}{1-\phi}\right)^{\beta} \tag{24}$$

where α and β are empirical parameters taking values of 4.1 and 2.96, respectively.

The required compressible tailings thickening bed structure parameters in the model calculation are summarized in Table 5. Based on the parameters in the table, we obtained the comparison of the simulation results with the empirical equations and the new model, as shown in Fig. 18(a) and Fig. 18(b), respectively.

Table 5 Model calculation parameters.

Sample	φ_c	ϕ	d_p (μm)	λ_{max} (μm)	D_f	D_T	α	β	D_c (μm)	T_w	L_s (μm)
0 rpm-28 cm	0.9990	0.646	22.9	877.3	2.56	1.306	4.1	2.96	147.3	5.50	1500
0 rpm-22 cm	0.9989	0.555	22.9	873.6	2.57	1.378	4.1	2.96	111.9	5.73	1500
0 rpm-12 cm	0.9985	0.508	22.9	446.8	2.55	1.382	4.1	2.96	57.5	8.21	1500
0 rpm-10 cm	0.9987	0.506	22.9	335.3	2.56	1.389	4.1	2.96	57.1	8.25	1500
0 rpm-8 cm	0.9984	0.490	22.9	328.6	2.55	1.388	4.1	2.96	56.1	8.48	1500

0 rpm-6 cm	0.9984	0.484	22.9	331.4	2.55	1.395	4.1	2.96	56.5	8.31	1500
0 rpm-4 cm	0.9979	0.478	22.9	329.3	2.55	1.396	4.1	2.96	53.8	8.54	1500
0rpm-2cm	0.9976	0.455	22.9	327.6	2.54	1.405	4.1	2.96	51.7	8.47	1500
1 rpm-24 cm	0.9964	0.518	22.9	692.3	2.69	1.295	4.1	2.96	122.2	6.15	1500
1 rpm-22 cm	0.9951	0.512	22.9	669.8	2.69	1.306	4.1	2.96	111.5	6.69	1500
1 rpm-12 cm	0.9945	0.403	22.9	346.6	2.65	1.395	4.1	2.96	53.2	8.60	1500
1 rpm-10 cm	0.9931	0.362	22.9	400.0	2.63	1.396	4.1	2.96	51.9	8.39	1500
1 rpm-8 cm	0.9930	0.347	22.9	376.5	2.62	1.398	4.1	2.96	53.2	8.58	1500
1 rpm-6 cm	0.9880	0.324	22.9	300.0	2.61	1.405	4.1	2.96	51.0	8.42	1500
1 rpm-4 cm	0.9749	0.302	22.9	295.2	2.58	1.407	4.1	2.96	48.7	8.77	1500
1 rpm-2 cm	0.9722	0.295	22.9	301.3	2.58	1.413	4.1	2.96	49.3	8.98	1500

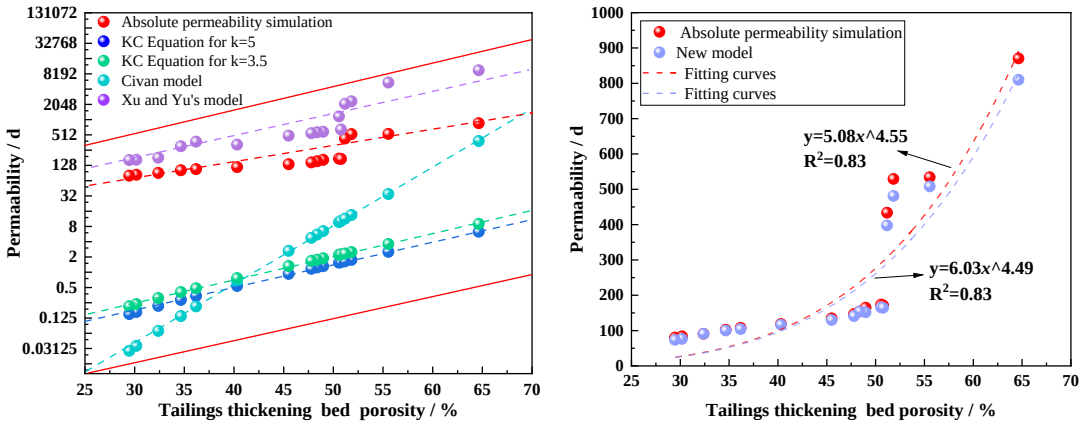

Fig. 18. Comparison results of compressible tailings thickening bed permeability: (a) Comparison of compressible tailings thickening bed permeability with empirical equations; (b) Comparison of compressible tailings thickening bed permeability with the new model.

Fig. 18(a) shows the simulated results of compressible tailings thickening bed permeability at different porosities compared with the empirical model. We find that the calculated results of the Xu and Yu models are much larger than the simulated results. The reason for this is that the fractal model calculates the compressible tailings thickening bed permeability using the parameter λ_{max}, the maximum pore diameter in the compressible tailings thickening bed pore structure [13]. We combined this with the analysis in Section 3.3, it can be seen that the pore structure in the compressible tailings thickening bed structure is non-uniform size, and the distribution range of pore diameter is wide. The fractal model is susceptible to the influence of the maximum pore diameter in calculating the compressible tailings thickening bed permeability, which results in

large errors. Therefore, the fractal model is still unsuitable for the permeability prediction of compressible tailings thickening bed. The predicted values of compressible tailings thickening bed permeability by the KC model are all lower than the simulation results, which is consistent with the conclusion of Feng's study [22]. Compared with the prediction result of k=5, the error of the prediction result of k=3.5 is decreasing. However, the KC model is still not suitable for the permeability prediction of compressible tailings thickening bed. The main reason is that in the KC model, the pore structure of the compressible tailings thickening bed is simplified to capillary bundles of the same diameter [10].

In the PNM model of the pore structure of compressible tailings thickening bed, the throat diameters that play a role in drainage are widely distributed, and the throat diameters are in change with the tailings thickening bed pressure and rake shear, which is challenging to be accurately quantified by a single k value. The calculation results of the Civan model showed that the predicted results were close to the simulated results only when the tailings thickening bed porosity was 64.6%. When the tailings thickening bed's porosity decreases, the Civan model's predicted results differ significantly from the simulated results. The main reason is that the Civan model is a power-law equation. The derivation process of the model simplifies the structural parameters, such as the equivalent diameter and tortuosity of the compressible tailings thickening bed pores, to the empirical parameters α and β of the power-law equation [12], which does not match the variation of the pore throat structure in the PNM model of compressible tailings thickening bed. Therefore, the Civan model with two empirical parameters is still not suitable for the permeability prediction of compressible tailings thickening bed.

Fig. 18(b) shows the simulated results of compressible tailings thickening bed permeability with different porosity compared with the new model. We can find that the prediction results of the new model for the permeability of the compressed tailings thickening bed are closer to the simulation results. Among the prediction results of the new model for the permeability of 16 tailings thickening beds, the prediction results of 10 data points are within the error region of ±5% of the simulation results, and the prediction results of 16 data points are within the error region of ±10% of the simulation results. The above data results indicate that the new model considering the throat structure parameter T_w predicts the compressible tailings thickening bed permeability more accurately than the empirical model.

3.6 Analysis of the influence of structural parameters of the throat on permeability

The equivalent diameter and length of the throat structure of the compressible tailings thickening bed are dynamic changes during the compression process. To clarify the effect of the variation of the throat structure on the compressible tailings thickening bed permeability, we plotted the variation of the compressible tailings thickening bed permeability with the average throat diameter and the average throat length with and without shear, as shown in Figs. 19(a) and 19(b), respectively.

We found that both the compressible tailings thickening bed permeability increased with the increase in pore throat diameter and length. The increase in pore throat diameter facilitates the discharge of fluid in the tailings thickening bed, thus increasing the permeability of the tailings thickening bed, which is consistent with the results of previous research [42]. Previous studies have shown that the increase in pore tortuosity in the compressible tailings thickening bed also increases the fluid channel length, which in turn increases the resistance to fluid discharge and adversely affects the permeability of the tailings thickening bed[38]. However, the data in Fig. 19(b) show that the permeability of the compressible tailings thickening bed increases with increasing throat length, which is inconsistent with the actual situation.

Fig. 19(c) depicts the variation of the throat length with the throat diameter. We found that when the throat diameter increased from 51.7 μm to 147.3 μm, the throat length also increased from 437.4 μm to 869.6 μm, and there was a linear relationship between them. The results also indicate that when considering the relationship between throat structure and tailings thickening bed permeability, the diameter and length of the throat cannot be considered alone. Therefore, this study proposes to use the dimensionless parameter T_w, the ratio of throat length to throat diameter, to measure the effect of throat structure changes on the compressible tailings thickening bed permeability. The relationship between the compressible tailings thickening bed permeability with and without shear and T_w is shown in Fig. 19(d). The compressible tailings thickening bed permeability decreases with increasing T_w, especially when the value of T_w is greater than 8. The decrease in the compressible tailings thickening bed permeability is more obvious. The analysis found that the smaller the T_w is, the more favorable the fluid transfer between two adjacent spherical pores, i.e., the smaller the T_w is, the more favorable the fluid discharge in the compressible tailings thickening bed. The increase in the T_w value indicates that the morphology

of the throat is more inclined to the elongated structure, which increases the difficulty of the fluid discharge in the compressible tailings thickening bed and is not conducive to the increase in the tailings thickening bed concentration.

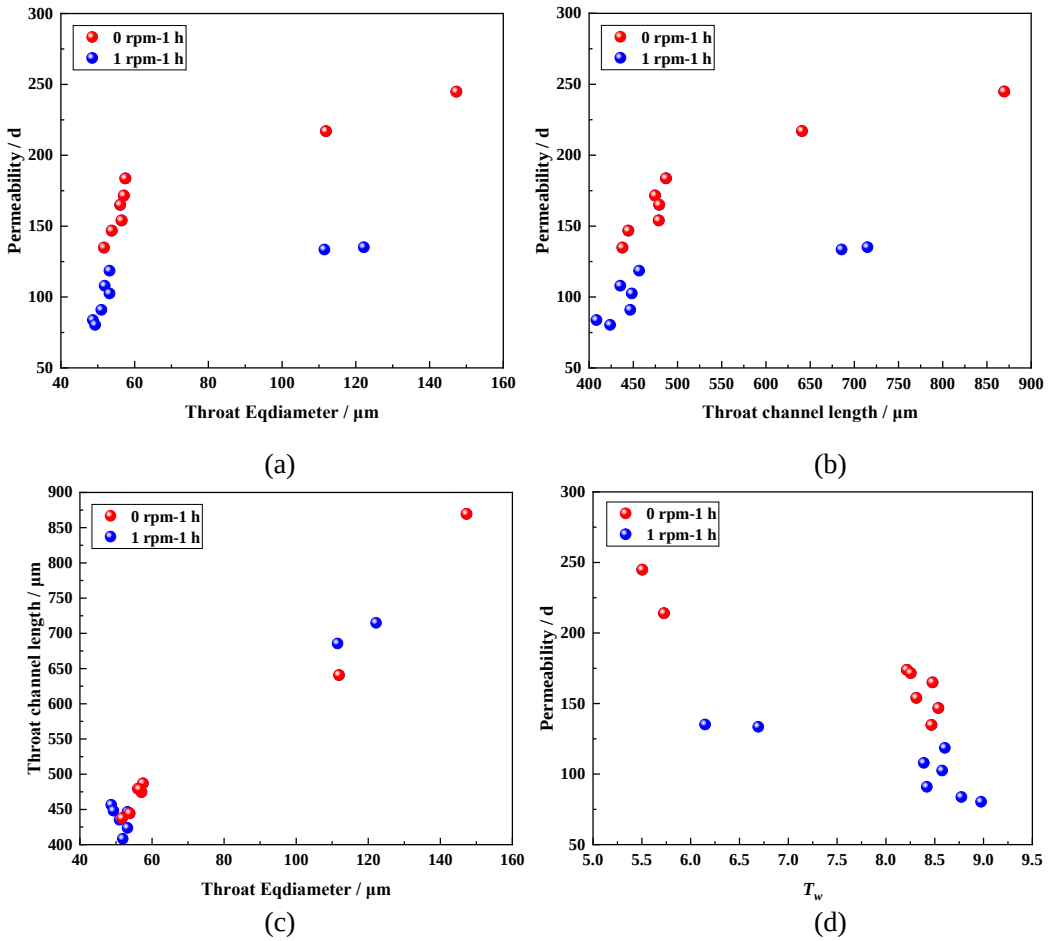

Fig. 19. Variation of compressible tailings thickening bed permeability with structural parameters of throat: (a) variation of compressible tailings thickening bed permeability with throat diameter; (b) variation of compressible tailings thickening bed permeability with throat length; (c) variation of throat length with diameter; (d) variation of compressible tailings thickening bed permeability with throat T_w.

Fig. 20(a) and Fig. 20(b) show the variation of the throat structure T_w value with throat diameter with and without shear, respectively. It can be seen that the variation trend of throat T_w values with throat diameter for different tailings thickening bed pressures is consistent, and both decrease with increasing throat diameter. This indicates that the throat structure with a larger diameter is more favorable for the drainage of water in the tailings thickening bed during the infiltration and drainage of the tailings thickening bed structure. The analysis of the T_w values of the throat structures at different tailings thickening bed heights revealed that different T_w values existed for throat structures of the same diameter. This again shows the inadequacy of considering only the influence of throat diameter or length on the permeability of the compressible tailings

thickening bed. It also verifies the reasonableness of the T_w value proposed in this study for the throat structure.

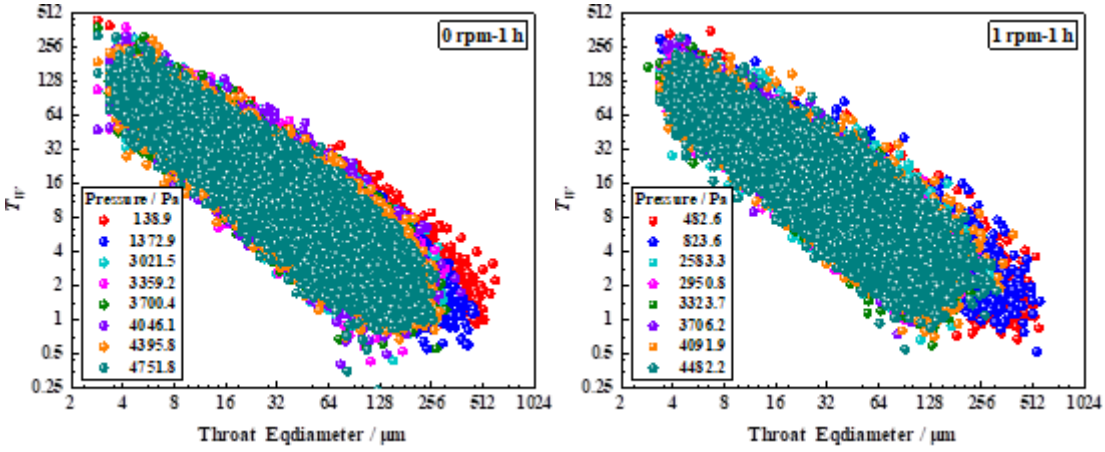

(a) (b)

Fig. 20. Variation of the structural parameter T_w with the diameter of the throat: (a) 0 rpm-1 h; (b) 1 rpm-1 h.

4. Conclusions

In this study, we obtained the pore structure of the compressible tailings thickening bed at different pressures with and without shear by computed tomography, respectively. The porosity, pore connectivity, spherical pore diameter, stick throat diameter, and stick throat length of the tailings thickening bed structure were also characterized based on the PNM model. Permeability simulation experiments of the compressible tailings thickening bed structure were carried out to analyze the permeability variation trend of the compressible tailings thickening bed structure. Based on the PNM model of the thickening bed pore structure and the thickening bed permeability research, a new permeability model was proposed considering the throat structure parameter T_w. The compressible tailings thickening bed permeability was predicted by three empirical models and compared with the simulation results and the new model.

The porosity of the compressible tailings thickening bed structure decreases as the tailings thickening bed pressure increases. The tailings particles complete isovolumetric exchange with the pore structure, increasing the tailings thickening bed slurry concentration. Compared with without shear, the rake shear causes forced destruction of the compressible tailings thickening bed pore structure, forcing further fluid discharge from the thickening bed and increasing the tailings thickening bed slurry concentration again.

The spherical pore diameter, stick throat diameter, and stick throat length decreases with

increasing tailings thickening bed pressure. The parameters of the stick throat structure constrain the drainage capacity of the compressible tailings thickening bed. Considering throat diameter or throat length alone does not accurately describe the relationship between compressible tailings thickening bed permeability and throat structure parameters. The T_w value considering the ratio of throat length to diameter, can more reasonably describe the relationship between the compressible tailings thickening bed permeability. And the tailings thickening bed permeability decrease with the increase in the throat T_w value.

The permeability of compressible tailings thickening bed decreases with increasing tailings thickening bed concentration, implying that it is difficult to increase the slurry concentration again with highly concentrated slurry under the same experimental conditions. The Xu and Yu, KC, and Civan models are less applicable to compressible tailings thickening bed permeability prediction. The new model considering the throat structure parameter T_w is more accurate for predicting compressible tailings thickening bed permeability. However, this study has yet to analyze the classification of primary and secondary percolation channels in the compressible tailings thickening bed based on the throat structure parameter T_w, which will be the focus of our subsequent work.

Acknowledgements

This work was funded by the National Key R&D Program of China (2022YFC2903803), the National Natural Science Foundation of China (no. 52130404), the Fundamental Research Funds for the Central Universities (no.FRF-TP-22-112A1), Guangdong Basic and Applied Basic Research Foundation (no. 2021A1515110161), Postdoctor Research Foundation of Shunde Graduate School of University of Science and Technology Beijing (no.2021BH011), ANID (Chile) through Fondecyt project 1210610, Centro de Modelamiento Matemático (BASAL funds for Centers of Excellence FB210005), CRHIAM project ANID/FONDAP/15130015, and Anillo project ANID/ACT210030.

Conflict of Interest

All the authors declare that there is no conflict of interests regarding the publication of this paper.

References

[1] Z. Feng, X. Dong, Y. Fan, H. Li, Y. Dong, X. Ma, R. Chen, Use of X-ray microtomography to quantitatively characterize the pore structure of three-dimensional filter cakes, Miner. Eng.

152 (2020) 106275. https://doi.org/10.1016/j.mineng.2020.106275.
[2] S. Prasertkulsak, C. Chiemchaisri, W. Chiemchaisri, K. Yamamoto, Removals of pharmaceutical compounds at different sludge particle size fractions in membrane bioreactors operated under different solid retention times, J. Hazard. Mater. 368 (2019) 124–132. https://doi.org/10.1016/j.jhazmat.2019.01.050.
[3] M. Bakraoui, Y. El Gnaoui, N. Lahboubi, F. Karouach, H. El Bari, Kinetic study and experimental productions of methane production from UASB reactor treating wastewater from recycled pulp and paper for the continuous test, Biomass Bioenergy. 139 (2020) 105604. https://doi.org/10.1016/j.biombioe.2020.105604.
[4] D. Kim, J.-H. Yu, K.-S. Hong, C.-D. Jung, H. Kim, J. Kim, S. Myung, Green production of low-molecular-weight xylooligosaccharides from oil palm empty fruit bunch via integrated enzymatic polymerization and membrane separation for purification, Sep. Purif. Technol. 293 (2022) 121084. https://doi.org/10.1016/j.seppur.2022.121084.
[5] D. Gomes, M.A.S. Correia, M.J. Romão, L.A. Passarinha, A. Sousa, Integrated approaches for the separation and purification of recombinant HPV16 E6 protein from Escherichia coli crude extracts, Sep. Purif. Technol. 315 (2023) 123647. https://doi.org/10.1016/j.seppur.2023.123647.
[6] D. Wang, D. Wang, X. Tan, A. Yeung, Q. Liu, A review of the roles of constituent minerals and residual bitumen in the solid-liquid separation of oil sands tailings, J. Hazard. Mater. 451 (2023) 131178. https://doi.org/10.1016/j.jhazmat.2023.131178.
[7] B. Mwewa, M. Tadie, S. Ndlovu, G.S. Simate, E. Matinde, Recovery of rare earth elements from acid mine drainage: A review of the extraction methods, J. Environ. Chem. Eng. 10 (2022) 107704. https://doi.org/10.1016/j.jece.2022.107704.
[8] G. Chen, C. Li, Z. Ruan, R. Bürger, H. Hou, Research on floc structure and physical properties based on pipeline flocculation, J. Water Process Eng. 53 (2023) 103627. https://doi.org/10.1016/j.jwpe.2023.103627.
[9] N.A. Toprak, O. Altun, Considering hydrocyclone operation for tailings dewatering purpose and its effects on product specifications of paste backfill operations, Miner. Eng. 173 (2021) 107176. https://doi.org/10.1016/j.mineng.2021.107176.
[10] P. Yang, Z. Wen, R. Dou, X. Liu, Permeability in multi-sized structures of random packed porous media using three-dimensional lattice Boltzmann method, Int. J. Heat Mass Transf. 106 (2017) 1368–1375. https://doi.org/10.1016/j.ijheatmasstransfer.2016.10.124.
[11] T. Bourbié, O. Coussy, B. Zinszner, M.C. Junger, Acoustics of porous media, J. Acoust. Soc. Am. 3080 (1992), https://doi.org/10.1121/1.402899.
[12] F. Civan, Scale effect on porosity and permeability: Kinetics, model, and correlation, Aiche. j. 47(2001), 271-287, https://doi.org/10.1002/aic.690470206.
[13] P. Xu, B. Yu, Developing a new form of permeability and Kozeny–Carman constant for homogeneous porous media by means of fractal geometry, Adv. water resour. 31 (2008), 74-81, https://doi.org/10.1016/j.advwatres.2007.06.003.
[14] L. Chen, A. He, J. Zhao, Q. Kang, Z.-Y. Li, J. Carmeliet, N. Shikazono, W.-Q. Tao, Pore-scale modeling of complex transport phenomena in porous media, Prog. Energy Combust. Sci. 88 (2022) 100968. https://doi.org/10.1016/j.pecs.2021.100968.
[15] H. Pape, C. Clauser, J. Iffland, Variation of Permeability with Porosity in Sandstone Diagenesis Interpreted with a Fractal Pore Space Model, in: T.G. Blenkinsop, J.H. Kruhl, M.

Kupková (Eds.), Fractals Dyn. Syst. Geosci., Birkhäuser Basel, Basel, 2000: pp. 603–619. https://doi.org/10.1007/978-3-0348-8430-3_8.

[16] M.N. Panda, L.W. Lake, Estimation of Single-Phase Permeability from Parameters of Particle-Size Distribution, AAPG Bull. 78 (1994) 1028–1039.

[17] G.A. Bayles, G.E. Klinzing, S.H. Chiang, Fractal mathematics applied to flow in porous systems, Part. Part. Syst. Char. 6 (1989), 168-175, https://doi.org/10.1002/ppsc.19890060128.

[18] N. Jeong, Advanced Study About the Permeability for Micro-Porous Structures Using the Lattice Boltzmann Method, Transp. Porous Media. 83 (2010) 271–288. https://doi.org/10.1007/s11242-009-9438-6.

[19] T. Tang, J.M. McDonough, A theoretical model for the porosity–permeability relationship, Int. J. Heat Mass Transf. 103 (2016) 984–996. https://doi.org/10.1016/j.ijheatmasstransfer.2016.07.095.

[20] Q. Dai, G. Wang, X. Zhao, Z. Han, K. Lu, J. Lai, S. Wang, D. Li, Y. Li, K. Wu, Fractal model for permeability estimation in low-permeable porous media with variable pore sizes and unevenly adsorbed water lay, Mar. Pet. Geol. 130 (2021) 105135. https://doi.org/10.1016/j.marpetgeo.2021.105135.

[21] X. Chen, G. Yao, An improved model for permeability estimation in low permeable porous media based on fractal geometry and modified Hagen-Poiseuille flow, Fuel. 210 (2017) 748–757. https://doi.org/10.1016/j.fuel.2017.08.101.

[22] Z. Feng, Y. Fan, X. Dong, X. Ma, R. Chen, Permeability estimation in filter cake based on X-ray microtomography and Lattice Boltzmann method, Sep. Purif. Technol. 275 (2021) 119114. https://doi.org/10.1016/j.seppur.2021.119114.

[23] F. Yu, D. Sun, M. Hu, J. Wang, Study on the pores characteristics and permeability simulation of pervious concrete based on 2D/3D CT images, Constr. Build. Mater. 200(2019), 687-702, https://doi.org/10.1016/j.conbuildmat.2018.12.135.

[24] W. He, J. Nan, H. Li, S. Li, Characteristic analysis on temporal evolution of floc size and structure in low-shear flow, Water Res. 46 (2012) 509–520. https://doi.org/10.1016/j.watres.2011.11.040.

[25] A. Wu, Z. Ruan, R. Bürger, S. Yin, J. Wang, Y. Wang, Optimization of flocculation and settling parameters of tailings slurry by response surface methodology, Miner. Eng. 156 (2020) 106488. https://doi.org/10.1016/j.mineng.2020.106488.

[26] E. Carissimi, J. Rubio, Polymer-bridging flocculation performance using turbulent pipe flow, Miner. Eng. 70 (2015) 20–25. https://doi.org/10.1016/j.mineng.2014.08.019.

[27] Z. Ruan, A. Wu, R. Bürger, F. Betancourt, Y. Wang, Y. Wang, H. Jiao, S. Wang, Effect of interparticle interactions on the yield stress of thickened flocculated copper mineral tailings slurry, Powder Technol. 392 (2021) 278–285. https://doi.org/10.1016/j.powtec.2021.07.008.

[28] C.K. Tan, J. Bao, G. Bickert, A study on model predictive control in paste thickeners with rake torque constraint, Miner. Eng. 105 (2017) 52–62. https://doi.org/10.1016/j.mineng.2017.01.011.

[29] X. Li, C. Li, Z. Ruan, B. Yan, H. Hou, L. Chen, Analysis of particle migration and agglomeration in paste mixing based on discrete element method, Constr. Build. Mater. 352 (2022) 129007. https://doi.org/10.1016/j.conbuildmat.2022.129007.

[30] Y. Wang, Z. Song, T. Mao, C. Zhu, Macro–Meso Fracture and Instability Behaviors of Hollow-Cylinder Granite Containing Fissures Subjected to Freeze–Thaw–Fatigue Loads,

Rock Mech. Rock Eng. 55 (2022) 4051–4071. https://doi.org/10.1007/s00603-022-02860-5.
[31] H. Jiao, S. Wang, Y. Yuan, X. Chen, Water recovery improvement by shearing of gravity-thickened tailings for cemented paste backfill, J. Clean. Prod. 245 (2020), 118882, https://doi.org/10.1016/j.jclepro.2019.118882.
[32] W. Yuan, W. Fan, Quantitative study on the microstructure of loess soils at micrometer scale via X-ray computed tomography, Powder Technol. 408 (2022) 117712. https://doi.org/10.1016/j.powtec.2022.117712.
[33] G. Liang, A.V. Nguyen, W. Chen, T.A.H. Nguyen, S. Biggs, Interaction forces between goethite and polymeric flocculants and their effect on the flocculation of fine goethite particles, Chem. Eng. J. 334 (2018) 1034–1045. https://doi.org/10.1016/j.cej.2017.10.107.
[34] V. Busignies, B. Leclerc, P. Porion, P. Evesque, G. Couarraze, P. Tchoreloff, Quantitative measurements of localized density variations in cylindrical tablets using X-ray microtomography, Eur. J. Pharm. Biopharm. 64 (2006) 38–50. https://doi.org/10.1016/j.ejpb.2006.02.007.
[35] N. Otsu, A Tlreshold Selection Method from Gray-Level Histograms, (n.d.).
[36] S. Liu, J.H. Masliyah, Single Fluid Flow in Porous Media, Chem. Eng. Commun. 148 (1996), 653–732, https://doi.org/10.1080/00986449608936537.
[37] D. Lasseux, F.J. Valdés-Parada, On the developments of Darcy's law to include inertial and slip effects, Comptes Rendus Mécanique. 345 (2017) 660–669. https://doi.org/10.1016/j.crme.2017.06.005.
[38] Y. Wang, C. Xie, Uniform Structural Stability of Hagen–Poiseuille Flows in a Pipe, Commun. Math. Phys. 393 (2022) 1347–1410. https://doi.org/10.1007/s00220-022-04389-8.
[39] S.J. Jackson, Q. Lin, S. Krevor, Representative Elementary Volumes, Hysteresis, and Heterogeneity in Multiphase Flow From the Pore to Continuum Scale, Water Resour. Res. 56 (2020) e2019WR026396. https://doi.org/10.1029/2019WR026396.
[40] H. Jiao, Y. Wu, H. Wang, X. Chen, Z. Li, Y. Wang, B. Zhang, J. Liu, Micro-scale mechanism of sealed water seepage and thickening from tailings bed in rake shearing thickener, Miner. Eng. 173 (2021) 107043. https://doi.org/10.1016/j.mineng.2021.107043.
[41] C. Li, G. Chen, Z. Ruan, R. Bürger, Y. Gao, H. Hou, H. Wang, Research on the effect of polar and azimuthal angle variations of coarse particles on the structure of drainage channels in the thickened bed, Int. J. Miner. Metall. Mater. (2023). https://doi.org/10.1007/s12613-023-2680-z.
[42] H. Jiao, Y. Wu, H. Wang, X. Chen, Z. Li, Y. Wang, B. Zhang, J. Liu, Micro-scale mechanism of sealed water seepage and thickening from tailings bed in rake shearing thickener, Miner. Eng. 173 (2021), 107043, https://doi.org/10.1016/j.mineng.2021.107043.
[43] X. Liu, M. Matti Maricq, D.A. Dobson, Statistical capillary tube model for porous filter media: An application in modeling of gasoline particulate filter, Sep. Purif. Technol. 286 (2022) 120393. https://doi.org/10.1016/j.seppur.2021.120393.
[44] B. Sutariya, S. Karan, A realistic approach for determining the pore size distribution of nanofiltration membranes, Sep. Purif. Technol. 293 (2022) 121096. https://doi.org/10.1016/j.seppur.2022.121096.